

# Strong competition between orbital-ordering and itinerancy in a frustrated spinel vanadate

J. Ma,<sup>1</sup> J. H. Lee,<sup>2</sup> S. E. Hahn,<sup>1</sup> Tao Hong,<sup>1</sup> H. B. Cao,<sup>1</sup> A. A. Aczel,<sup>1</sup> Z. L. Dun,<sup>3</sup> M. B. Stone,<sup>1</sup> W. Tian,<sup>1</sup> Y. Qiu,<sup>4,5</sup> J. R. D. Copley,<sup>4</sup> H. D. Zhou,<sup>3</sup> R. S. Fishman,<sup>2,\*</sup> and M. Matsuda<sup>1</sup>

<sup>1</sup>*Quantum Condensed Matter Division, Oak Ridge National Laboratory, Oak Ridge, Tennessee 37831, USA*

<sup>2</sup>*Materials Science and Technology Division, Oak Ridge National Laboratory, Oak Ridge, Tennessee, 37831, USA*

<sup>3</sup>*Department of Physics and Astronomy, University of Tennessee, Knoxville, Tennessee 37996, USA*

<sup>4</sup>*NIST Center for Neutron Research, Gaithersburg, Maryland 20899-6102, USA*

<sup>5</sup>*Department of Materials Science and Engineering, University of Maryland, College Park, Maryland 20742, USA*

The crossover from localized- to itinerant-electron regimes in the geometrically-frustrated spinel system  $\text{Mn}_{1-x}\text{Co}_x\text{V}_2\text{O}_4$  is explored by neutron-scattering measurements, first-principles calculations, and spin models. At low Co doping, the orbital ordering (OO) of the localized  $\text{V}^{3+}$  spins suppresses magnetic frustration by triggering a tetragonal distortion. At high Co doping levels, however, electronic itinerancy melts the OO and lessens the structural and magnetic anisotropies, thus increases the amount of geometric frustration for the V-site pyrochlore lattice. Contrary to the predicted paramagnetism induced by chemical pressure, the measured noncollinear spin states in the Co-rich region of the phase diagram provide a unique platform where localized spins and electronic itinerancy compete in a geometrically-frustrated spinel.

PACS numbers: 61.05.fm, 75.10.Jm, 75.25.Dk, 75.30.Et

The competition between localized and itinerant behavior triggers many intriguing phenomena such as metal-insulator transitions [1], colossal magnetoresistance [2], and superconductivity in heavy fermion [3] and Fe-based materials [4]. Likewise, the transformation from itinerant to localized spins in geometrically-frustrated systems can create exotic phases by modifying the relationship between the spin, orbital, and lattice [5] degrees of freedom. Although the competing effects of localized and itinerant behavior on magnetic frustration have been rather extensively investigated on triangular and pyrochlore lattices, they have rarely been explored for the frustrated spinel  $\text{AB}_2\text{O}_4$ .

Underlying the rich phase diagrams of spinels are the tuneable magnetic interactions between the *A* and *B* sites and the geometric frustration experienced by the *B* sites on a pyrochlore lattice. Spinel vanadates exhibit additional intriguing characteristics due to the orbital ordering (OO) [6–12] of the partially-filled ( $3d^2$ ) *B*-sites. Because itinerancy interferes with OO [9–13], it enriches the complex interplay between the magnetic, orbital, and lattice degrees of freedom. But this complexity also makes it difficult to provide a detailed microscopic understanding of this system [8, 14–18]. Through substitution of the *A*-site, we systematically study the competition between OO and itinerancy in the spinel vanadates. In particular, the modified spin, orbital, and lattice couplings in  $\text{Mn}_{1-x}\text{Co}_x\text{V}_2\text{O}_4$  are used to reveal the competing effects of OO and itinerancy on the coupled magnetic and structural phase transitions [13, 19, 20].

Elastic and inelastic neutron-scattering (INS) measurements are combined with first-principles calculations and spin models to study single-crystals of  $\text{Mn}_{1-x}\text{Co}_x\text{V}_2\text{O}_4$ .

Because  $\text{Co}^{2+}$  is the smallest 2+ magnetic cation that can be introduced on the *A* site, it exerts strong chemical pressure. Previously, this chemical pressure was expected to induce itinerancy and consequent paramagnetism [13]. However, we find that the itinerancy driven by Co doping unexpectedly enhances both the para-to-collinear and collinear-to-noncollinear (CL to NC) transition temperatures,  $T_{\text{CL}}$  and  $T_{\text{NC}}$ . While the magnetic ground state of the V spins remains a two-in/two-out state throughout the entire doping range, that state has different origins in the itinerant (Co-rich) and localized (Co-poor) regimes.

At low Co doping, OO suppresses frustration by triggering cubic-to-tetragonal structural and CL to NC (two-in/two-out) magnetic transitions at  $T_S = T_{\text{NC}}$ . However, at high Co doping, itinerancy weakens the structural transition ( $T_S < T_{\text{NC}}$ ) by melting the OO and revives the suppressed frustration. Despite the complete disappearance of OO and of the structural transition, the novel two-in/two-out is stabilized by the revived frustration and the enhanced Co-V exchange at an even higher temperature than at low doping levels.

Neutron-diffraction experiments were performed at the four-circle diffractometer (HB-3A) and the triple-axis spectrometer (HB-1A) at the High Flux Isotope Reactor (HFIR) of the Oak Ridge National Laboratory (ORNL). The data were refined by the Rietveld method using FULLPROF [21]. INS data were collected utilizing the thermal (HB-1) and cold (CG-4C) triple-axis spectrometers at HFIR, ORNL, with fixed final energies of 14.7 meV at HB-1 and 5 or 3.5 meV at CG-4C, respectively; and the time-of-flight (tof) spectrometers, DCS, at National Institute of Standards and Technology (NIST) [22] and SEQUOIA, at the Spallation Neutron Source (SNS)

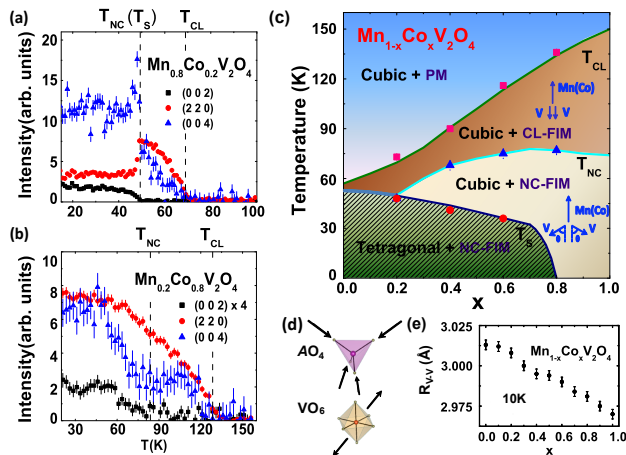


FIG. 1. (color online) Temperature dependence of the Bragg peaks, (002) (squares), (220) (circles), and (004) (triangles) in (a)  $\text{Mn}_{0.8}\text{Co}_{0.2}\text{V}_2\text{O}_4$  and (b)  $\text{Mn}_{0.2}\text{Co}_{0.8}\text{V}_2\text{O}_4$ . The background has been subtracted. (c) The temperature versus Co-doping content ( $x$ ) phase diagram. The para-to-CL magnetic transition temperature  $T_{CL}$ , the CL-NC ferrimagnetic phase transition temperature  $T_{NC}$ , and the cubic-to-tetragonal lattice transition temperature  $T_S$  are determined from the magnetic susceptibility/heat capacity (solid lines) and neutron-scattering experiments (square, triangle, and circle for the transitions). (d)  $\text{AO}_4$  ( $A=\text{Mn}^{2+}/\text{Co}^{2+}$ ) tetrahedron and  $\text{VO}_6$  octahedron. (e) The  $x$  dependence of the  $\text{V}^{3+}$ - $\text{V}^{3+}$  distance,  $R_{V-V}$ , at 10 K (black dots).

with fixed incident energies of 25.25 and 30 meV, respectively. The tof data were analyzed with DAVE [23]. Error bars in the figures represent one standard deviation.

The Co-doping dependence of the crystal and magnetic structures and OO was determined by single-crystal neutron-diffraction measurements. Figures 1(a) and (b) show the temperature dependence of the (002), (220), and (004) Bragg peaks for  $\text{Mn}_{1-x}\text{Co}_x\text{V}_2\text{O}_4$  ( $x=0.2$  and  $0.8$ ). A ferrimagnetic (FIM) signal develops below  $T_{CL}$  at the symmetry-allowed Bragg positions (220) and (004). While the (002) peak is forbidden by symmetry, the observed scattering intensity below  $T_{NC}$  signals the formation of an antiferromagnetic (AFM) spin structure in the  $ab$ -plane. The onset of the (002) magnetic reflection marks the CL-NC magnetic transition at  $T_{NC}$ . The (004) reflection, which also increases in intensity below  $T_{NC}$ , provides a measure of both magnetic transitions. For  $x=0.2$ , the intensities of the (220) and (004) Bragg peaks rise at  $\sim 70$  K ( $T_{CL}$ ) due to the para-to-CL magnetic transition. The (220) peak drops sharply at  $\sim 50$  K ( $T_S=T_{NC}$ ) due to the cubic-to-tetragonal structural transition. Hence,  $T_{NC}$  coincides with  $T_S$  through  $x \approx 0.2$  [6]. For  $x > 0.2$ , the two transitions separate with  $T_S < T_{NC}$ . At  $x=0.8$ , the structural transition disappears, while two magnetic transitions are observed with  $T_{CL} \sim 150$  K and  $T_{NC} \sim 80$  K. In high Co-doped compounds, x-ray diffraction and heat capacity measurements also suggest the

absence of a structural transition [20].

To summarize the results as shown in the phase diagram in Fig. 1(c): we find for i)  $x \leq 0.2$ : a para-to-CL magnetic transition at  $T_{CL}$  and a cubic-to-tetragonal structural transition that coincides with the CL-NC transition at  $T_S = T_{NC} < T_{CL}$ ; ii)  $0.2 < x < 0.8$ : the CL-NC and cubic-to-tetragonal transitions are decoupled with  $T_S < T_{NC} < T_{CL}$ ; iii)  $x \geq 0.8$ : no structural transition is observed down to 5 K but two magnetic phase transitions appear with  $T_{NC} < T_{CL}$ . Both  $T_{CL}$  and  $T_{NC}$  increase while  $T_S$  gradually decreases with  $\text{Co}^{2+}$  doping. The detailed measurements used to map the phase diagram are provided in Supplementary Information(SI) A and B [24].

The microscopic effect of Co doping can be understood by considering the structures of the  $\text{AO}_4$  tetrahedra and  $\text{VO}_6$  octahedra. In the high-temperature cubic phase ( $Fd\bar{3}m$ ), the interior angles of the  $\text{AO}_4$  tetrahedra are  $\angle\text{O-A-O}=109.7^\circ$ . With Co doping, the A-O bond length decreases from 2.041 Å ( $x=0$ ) to 1.984 Å ( $x=0.8$ ), thereby applying chemical pressure along the A-O direction, Fig. 1(d). Each  $\text{VO}_6$  octahedra stretches along the  $\langle 111 \rangle$  direction, producing the local trigonal distortion shown in Fig. 1(d). Due to this distortion, the twelve O-V-O interior angles in the  $\text{VO}_6$  octahedra split away from  $90^\circ$  into two different angles. With  $\text{Co}^{2+}$  doping, the difference between the two O-V-O angles decreases from  $12.3(2)^\circ$  ( $x=0$ ) to  $10.0(2)^\circ$  ( $x=0.8$ ). Simultaneously, the V-O bond length shrinks from 2.023(1) Å ( $x=0$ ) to 2.012(1) Å ( $x=0.8$ ) and the V-V bond length ( $R_{V-V}$ ) shrinks from 3.013 to 2.975 Å, which increases both chemical pressure and structural isotropy.

The structural phase diagram reflects the evolution of these bond length and angle parameters with Co doping. Although the crystal space group changes from  $Fd\bar{3}m$  (cubic) to  $I4_1/a$  (tetragonal) with decreasing temperature when  $x < 0.8$ , it remains  $Fd\bar{3}m$  (cubic) down to the lowest temperature studied when  $x \geq 0.8$ . By contrast, most spinel vanadates exhibit structural transitions with decreasing temperature[6–12], so the behavior of the  $x \geq 0.8$  samples is anomalous.

On the other hand, magnetic structures is tightly coupled to the crystal structure and very sensitive to the Co doping level. Below  $T_{CL}$ , the Mn/Co moments are aligned parallel to the  $c$  axis. Above  $T_{NC}$ , the  $\text{V}^{3+}$  moments point along the  $c$  axis and antiparallel to the Mn/Co moments. Below  $T_{NC}$ , the  $\text{V}^{3+}$  moments form the two-in/two-out configuration observed previously in  $\text{MnV}_2\text{O}_4$  [25] and  $\text{FeV}_2\text{O}_4$  [26]. The canting of the  $\text{V}^{3+}$  moments away from the  $c$  axis starts below 70 K and reaches  $22.1(1.8)^\circ$  at 10 K for  $x=0.8$ , smaller than  $35.7(1.5)^\circ$  and  $36.2(1.5)^\circ$  for  $x=0.0$  and  $0.2$  at 10 K, respectively. Meanwhile, the  $\text{V}^{3+}$  ordered moment initially increases from  $0.95(4)\mu_B$  ( $x=0.0$ ) to  $1.03(7)\mu_B$  ( $x=0.2$ ), then decreases to  $0.61(3)\mu_B$  ( $x=0.8$ ) at 10 K. The enhancement of the  $\text{V}^{3+}$  moment from  $x = 0.0$  to  $0.2$  clearly

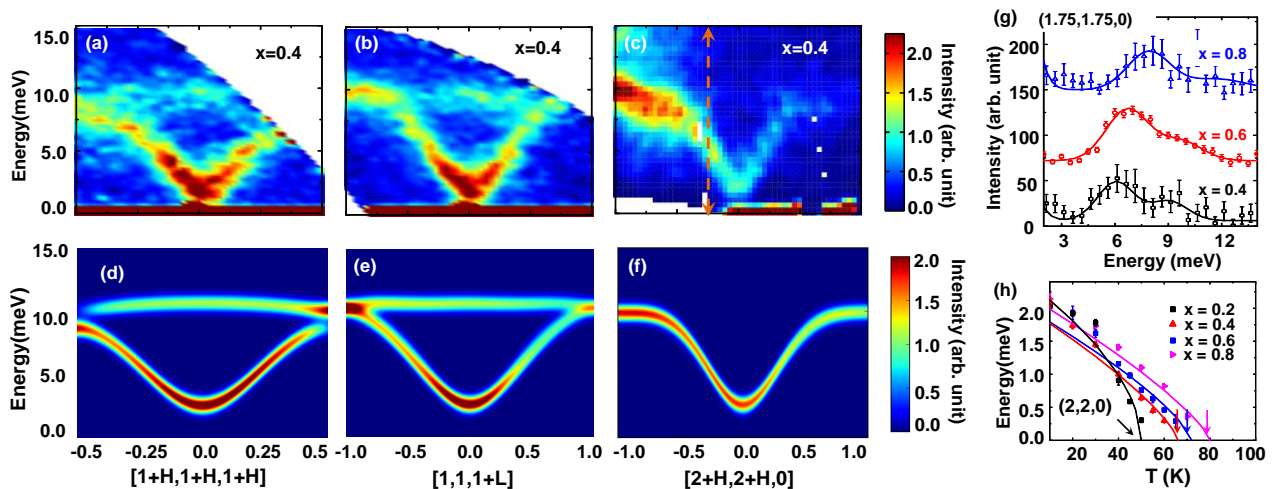


FIG. 2. (color online) (a)-(c) INS results for the magnetic excitations of  $\text{Mn}_{0.6}\text{Co}_{0.4}\text{V}_2\text{O}_4$  at 8 K. (d)-(f) The calculated excitation using the Hamiltonian, Eq. (1). The arrow line in (c) represents the position of the constant- $Q$  cut. (g) The constant- $Q$  cuts at  $(1.75, 1.75, 0)$  along  $[\text{H H } 0]$  direction in  $\text{Mn}_{1-x}\text{Co}_x\text{V}_2\text{O}_4$  measured at 8K,  $x=0.4, 0.6$  and  $0.8$ . The curves in (g) are Gaussian fits and guides to the eye. Note that the low-energy spin-wave branch hardens with Co-doping. (h) The spin-wave energy gap at the magnetic zone center  $(2, 2, 0)$  in  $\text{Mn}_{1-x}\text{Co}_x\text{V}_2\text{O}_4$ . The curves in (h) are power-law fits.

reflects the reduced orbital moment associated with Co doping. Contrary to the prediction that the small  $\text{Co}^{2+}$  cation triggers paramagnetism [13], we find that the ordered V magnetic moment does not disappear for Co-rich ( $x \geq 0.8$ ) compounds and their ordering temperatures ( $T_{CL}, T_{NC}$ ) even increase with doping, as shown in Fig. 1(c).

To confirm the itinerancy-induced origin of the NC states, the exchange interactions and anisotropies were evaluated from the INS spectra of spin-wave excitations. Since the interaction between the  $A^{2+}$  ions is known to be small [27–29], the interactions between the  $A^{2+}$  and  $V^{3+}$  ions can be estimated from the dispersion of the low-energy acoustic mode. For  $x=0.4$ , the measured dispersions along the  $\langle 110 \rangle$  direction are plotted in Fig. 2(a). Notice that two magnetic modes have been observed, as shown in Fig. 2(c), which is the same as in  $\text{MnV}_2\text{O}_4$  [29], and the spin-wave velocities increase with Co doping. Measured at the  $(220)$  zone center, the spin-wave gap is plotted as a function of temperature and doping in Fig. 2(d). As in  $\text{MnV}_2\text{O}_4$  [25] and  $\text{FeV}_2\text{O}_4$  [26], the spin-wave gap below  $T_{NC}$  is produced by easy-axis anisotropy along the cubic diagonal of each V tetrahedron, which also cants the  $V^{3+}$  moments away from the  $c$  axis. Intriguingly, this spin-wave gap is almost independent of Co-doping, Fig. 2(d). Ignoring  $J_{BB}^{ab}$  and  $J_{BB}^c$ , the spin-wave gap would be proportional to  $\sqrt{J_{AB} \times D_B}$ . We conclude that a roughly constant spin-wave gap of about 2 meV is maintained by the balance between the enhanced  $J_{AB}$  and the suppressed  $D_B$  associated with the itinerancy of the  $V^{3+}$  ions. In particular, the suppressed  $D_B$  promotes frustration in the spinel structure [30].

Spin-wave theory (SWT) was used to understand the

microscopic origin of the itinerancy-driven NC states in the absence of OO. These calculations were based on the Hamiltonian with six inequivalent sublattices,

$$\begin{aligned}
 H = & -J_{AB} \sum_{(p,q)(i,j,k,l)} (\mathbf{S}_p + \mathbf{S}_q) \cdot (\mathbf{S}_i + \mathbf{S}_j + \mathbf{S}_k + \mathbf{S}_l) \\
 & - J_{BB}^{ab} \left( \sum_{i,j} \mathbf{S}_i \cdot \mathbf{S}_j + \sum_{k,l} \mathbf{S}_k \cdot \mathbf{S}_l \right) \\
 & - J_{BB}^c \sum_{(i,j)(k,l)} (\mathbf{S}_i + \mathbf{S}_j) \cdot (\mathbf{S}_k + \mathbf{S}_l) \\
 & + D_A \sum_{r=p,q} (\hat{z} \cdot \mathbf{S}_r)^2 + D_B \sum_{s=i,j,k,l} (\hat{u}_s \cdot \mathbf{S}_s)^2 \quad (1)
 \end{aligned}$$

The inequivalent  $A$ -sites are given by subscripts  $p$  and  $q$ , and the inequivalent  $B$ -sites are given by subscripts  $i, j, k$  and  $l$ . Isotropic exchange constants ( $J_{AB}$ ,  $J_{BB}^{ab}$ , and  $J_{BB}^c$ ) describe nearest-neighbor interactions, Fig. 3(c). For the  $A$ -site spins, the easy-axis anisotropy,  $D_A$ , is along the  $c$ -axis while for the  $B$ -site spins, the easy-axis anisotropy,  $D_B$ , is along the local  $\langle 111 \rangle$  direction ( $\hat{u}_s$ ). A range of values for  $S_B$  and  $J_{BB}^{ab}$  produces fits of similar quality, (SI C.2) [24]. Parameters best describing the experimental data for  $\text{Mn}_{0.6}\text{Co}_{0.4}\text{V}_2\text{O}_4$  with  $S_A = 4.2 \mu_B$ ,  $S_B = 1.4 \mu_B$  and  $J_{BB}^{ab} = -8.0$  meV were  $J_{AB} = -1.8$  meV,  $J_{BB}^c = 1.1$  meV,  $D_B = -9.1$  meV and  $D_A = 0.4$  meV.

The simulated dispersions of  $\text{Mn}_{0.6}\text{Co}_{0.4}\text{V}_2\text{O}_4$  agree well with the measurements, Fig. 2. With Co doping, we fix the  $B$ -site (V) moment while lowering the  $A$ -site (Mn/Co) moment. As a result, the exchange  $J_{AB}$  for  $\text{Mn}_{0.6}\text{Co}_{0.4}\text{V}_2\text{O}_4$  is stronger than for  $\text{MnV}_2\text{O}_4$  (SI C.2) [24]. By inducing electronic itinerancy, density-functional

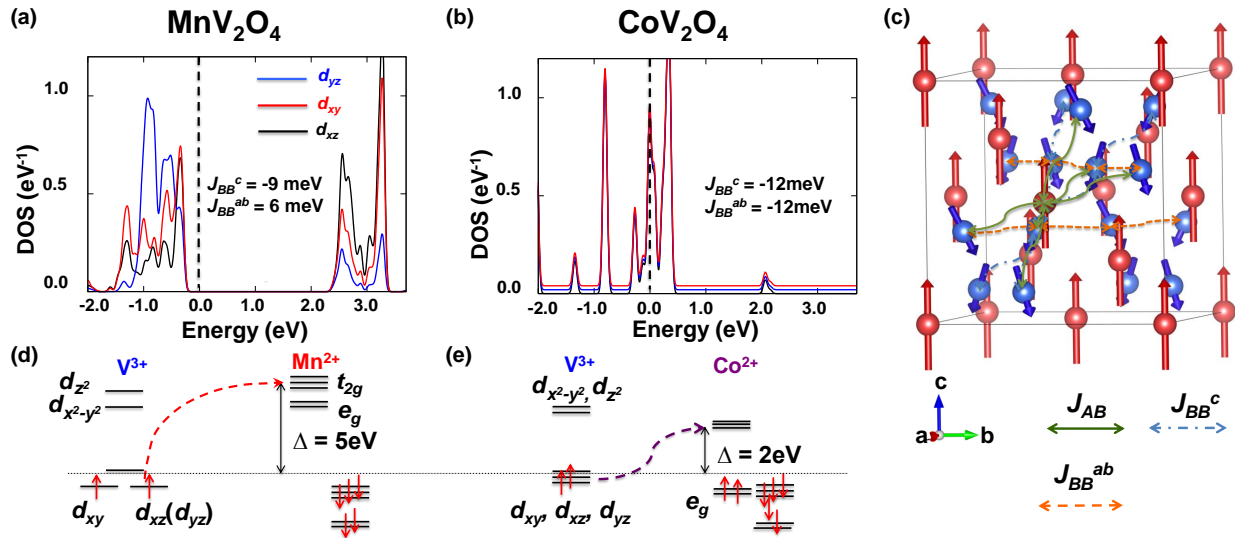


FIG. 3. (color online) (a) and (b) Density-of-states for AFM  $\text{MnV}_2\text{O}_4$  and  $\text{CoV}_2\text{O}_4$ , respectively. (c) NC state of  $\text{Mn}_{1-x}\text{Co}_x\text{V}_2\text{O}_4$ .  $J_{AB}$ ,  $J_{BB}^{ab}$ , and  $J_{BB}^c$  are the exchange interactions between nearest-neighbor sites. (d) and (e) Orbital energies estimated from DFT calculations.  $|J_{A-V}|$  is inversely proportional to the energy gap,  $\Delta$ . Only up-spin energy levels are shown for  $\text{V}^{3+}$  for simplicity.

theory (DFT) indicates that Co doping also strengthens both the structural ( $c \sim a$ ) and magnetic ( $J_{BB}^{ab} \sim J_{BB}^c$ ) isotropies, as shown in Figs. 3(a) and (b). If the  $J_{AB}$  interactions were not enhanced by Co doping, the remanent magnetic anisotropies along the diagonals of the V tetrahedra would transform the V spin state into an all-in/all-out structure. Due to the enhanced  $J_{AB}$ , however, the ground state of the V spins remains the same isosymmetric two-in/two-out state found for small Co doping.

With the orbital energies of both the A and B ions estimated from DFT (SI. D) [24], the origin of the enhanced  $J_{AB}$  is explained in Fig. 3(d) and (e). The large energy difference ( $\sim 5$  eV) between the occupied V and Mn  $d$  states weakens the exchange between Mn and V. By filling the  $e_g$  level, Co doping significantly lowers the  $t_{2g}$  level and enhances the exchange interaction between Co and V. DFT calculations reveal that the AFM  $J_{AB}$  is significantly enhanced in  $\text{CoV}_2\text{O}_4$  ( $-2.5$  meV) compared to  $\text{MnV}_2\text{O}_4$  ( $-1.2$  meV). Although the V electrons are delocalized by Co doping, the enhanced  $J_{AB}$  causes  $T_{CL}$  to grow. Further, the enhanced magnetic exchange isotropy ( $J_{BB}^{ab} \sim J_{BB}^c$ ) driven by orbital quenching (Fig 3(b)) stabilizes the isosymmetric NC phase and raises  $T_{NC}$ . Therefore, the induced itinerancy strengthens both the CL and NC phases even without OO.

Induced itinerancy is closely related to  $R_{V-V}$ . At 10 K, Fig. 1(e) shows that  $R_{V-V}$  remains almost constant up until  $x = 0.2$ , then begins to decrease. Based on our DFT calculations, the shorter  $R_{V-V}$  induces itinerant electronic behavior, as shown in Figs. 3(a) and (b), thereby suppressing OO. Due to the disappearance of OO by the itinerancy,  $T_S$  falls with Co doping.

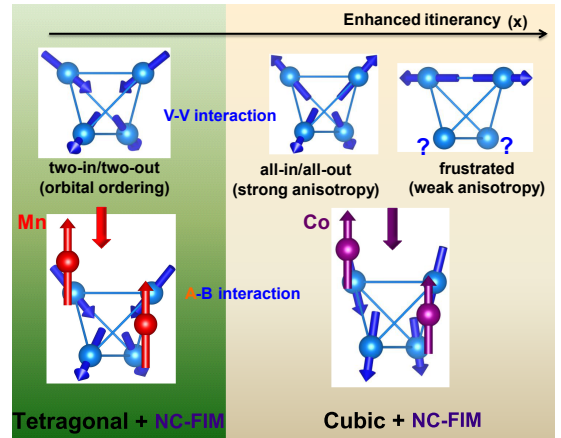


FIG. 4. (color online) The hierarchical magnetic states with V-V and V-Mn/Co interactions and the distinct origins of isosymmetric phase transition with Co-doping ( $x$ ).

As outlined in Fig. 4, the isosymmetric NC states have distinct origins for low and high  $x$ . For low Co-doping, the OO of the V ions relieves the magnetic frustration by triggering a tetragonal structure transition ( $c/a < 1$ ) and induces the two-in/two-out spin state. The Mn-V interactions only increase the canting angle while maintaining the two-in/two-out. If only the isotropic V-V interactions and the remanent local V anisotropy were considered, Co doping would produce an all-in/all-out spin state. However, the strong AFM  $J_{AB}$  between the Co and V sites stabilizes the observed two-in/two-out state in the high Co-doping compounds. Perturbations such as pressure may further strengthen the electronic itinerancy, weaken-

ing the remanent anisotropy and enhancing the magnetic frustration.

To summarize,  $\text{Mn}_{1-x}\text{Co}_x\text{V}_2\text{O}_4$  exhibits a rich phase diagram due to the crossover from localized to itinerant electronic regimes. The crystallographic and magnetic structures of compounds with low and high Co doping levels have different physical origins. At low Co doping, OO triggers a cubic-to-tetragonal lattice distortion, accompanied by a CL-to-NC magnetic transition. Co doping contracts  $R_{V-V}$ , enhances the electronic itineracy, and revives the magnetic frustration of the pyrochlore lattice by weakening the magnetic and structural anisotropies. With further Co doping, OO completely disappears and the magnetic ordering temperatures  $T_C$  and  $T_{NC}$  are driven higher by the enhanced exchange interaction  $J_{AB}$ . Since  $\text{CoV}_2\text{O}_4$  is located at the crossover between localized and itinerant electron behavior, external pressure may further strengthen itinerancy and magnetic isotropy, enhance geometric frustration, and produce other exotic behavior. The present results provide a microscopic picture for the competition between OO and electronic itineracy in this frustrated spinel series and suggest a new methodology for studying competing effects with multiple order parameters.

The research at HFIR and SNS, ORNL, were sponsored by the Scientific User Facilities Division (J.M., J.H.L, S.E.H., T.H., H.B.C., A.A.A., M.S., W.T., M.M.) and Materials Science and Engineering Division (J.H.L., R.F.), Office of Basic Energy Sciences, US Department of Energy. S.E.H. acknowledges support by the Laboratory's Director's fund, ORNL. Z.L.D and H.D.Z. thank the support from NSF-DMR through award DMR-1350002. Work at NIST is supported in part by the National Science Foundation under Agreement No. DMR-0944772. The authors acknowledge valuable discussions with S. Okamoto and G. MacDougall.

---

\* author to whom correspondences should be addressed: fishmanrs@ornl.gov and matsudam@ornl.gov

- [1] M. Imada, A. Fujimori, and Y. Tokura, *Rev. of Mod. Phys.* **70**, 1039 (1998).
- [2] A. P. Ramirez, *J. Phys.: Condens. Matter* **9**, 8171 (1997).
- [3] G. R. Stewart, *Rev. of Mod. Phys.* **56**, 755 (1984).
- [4] Y. Kamihara, H. Hiramatsu, M. Hirano, R. Kawamura, H. Yanagi, T. Kamiya, H. Hosono, *J. Am. Chem. Soc.* **128**, 10012 (2006).
- [5] C. Lacroix, P. Mendels, and F. Mila, *Introduction to Frustrated Magnetism: Materials, Experiments, Theory.* (Springer, 2001); S. Nakatsuji, Y. Machida, Y. Maeno, T. Tayama, T. Sakakibara, J. van Duijn, L. Balicas, J. N. Millican, R. T. Macaluso, and Julia Y. Chan, *Phys. Rev. Lett.* **96**, 087204 (2006); S. Kumar and J. van den Brink, *Phys. Rev. Lett.* **105**, 216405 (2010); H. Ishizuka and Y. Motome, *Phys. Rev. Lett.* **108**, 257205 (2012); M. Udagawa, H. Ishizuka, and Y. Motome, *Phys. Rev. Lett.* **108**, 066406 (2012); S.-B. Lee, A. Paramakanti, and Y. B. Kim, *Phys. Rev. Lett.* **111**, 196601 (2013).
- [6] V. O. Garlea, R. Jin, D. Mandrus, B. Roessli, Q. Huang, M. Miller, A. J. Schultz, and S. E. Nagler, *Phys. Rev. Lett.* **100**, 066404 (2008).
- [7] G. J. MacDougall, I. Brodsky, A. A. Aczel, V. O. Garlea, G. E. Granroth, A. D. Christianson, T. Hong, H. D. Zhou, and S. E. Nagler, *Phys. Rev. B* **89**, 224404 (2014).
- [8] T. Katsufuji, T. Suzuki, H. Takei, M. Shingu, K. Kato, K. Osaka, M. Takata, H. Sagayama, and T.-H. Arima, *J. Phys. Soc. Jpn.* **77**, 053708 (2008).
- [9] N. Nishiguchi and M. Onoda, *J. Phys. Condens. Matter* **14**, L551 (2002).
- [10] S. H. Lee, D. Louca, H. Ueda, S. Park, T. J. Sato, M. Isobe, Y. Ueda, S. Rosenkranz, P. Zschack, J. Íñiguez, Y. Qiu, and R. Osborn, *Phys. Rev. Lett.* **93**, 156407 (2004).
- [11] E. M. Wheeler, B. Lake, A. T. M. N. Islam, M. Reehuis, P. Steffens, T. Guidi, and A. H. Hill, *Phys. Rev. B* **82**, 140406(R) (2010).
- [12] A. Kismarhardja, J. S. Brooks, H. D. Zhou, E. S. Choi, K. Matsubayashi, and Y. Uwatoko, *Phys. Rev. B* **87**, 054432 (2013).
- [13] S. Blanco-Canosa, F. Rivadulla, V. Pardo, D. Baldomir, J.-S. Zhou, M. García-Hernández, M. A. López-Quintela, J. Rivas, and J. B. Goodenough, *Phys. Rev. Lett.* **99**, 187201 (2007).
- [14] S. Di Matteo, G. Jackeli, and N. B. Perkins, *Phys. Rev. B* **72**, 020408(R) (2005).
- [15] H. Tsunetsugu, and Y. Motome, *Phys. Rev. B* **68**, 060405(R) (2003).
- [16] Gia-Wei Chern, Natalia Perkins, and Zhihao Hao, *Phys. Rev. B* **81**, 125127 (2010).
- [17] S. Sarkar, T. Maitra, Roser Valentí, and T. Saha-Dasgupta, *Phys. Rev. Lett.* **102**, 216405 (2009).
- [18] K. Myung-Whun, S. Y. Jang, T. Katsufuji, and A. V. Boris, *Phys. Rev. B* **85**, 224423 (2012).
- [19] A. Kismarhardja, J. S. Brooks, A. Kiswandhi, K. Matsubayashi, R. Yamanaka, Y. Uwatoko, J. Whalen, T. Siegrist, and H. D. Zhou, *Phys. Rev. Lett.* **106**, 056602 (2011).
- [20] A. Kiswandhi, J. S. Brooks, J. Lu, J. Whalen, T. Siegrist, and H. D. Zhou, *Phys. Rev. B* **84**, 205138 (2011).
- [21] J. Rodriguez-Carvajal, Recent advances in magnetic structure determination by neutron powder diffraction. *Physica B* **192**, 55 (1993).
- [22] J. R. D. Copley and J. C. Cook, *Chem. Phys.* **292**, 477 (2003).
- [23] R. T. Azuah, L. R. Kneller, Y. Qiu, P. L. W. Tregenna-Piggott, C. M. Brown, J. R. D. Copley, and R. M. Dimeo, *J. Res. Natl. Inst. Stan. Technol.* **114**, 341 (2009).
- [24] See Supplemental Material at [URL will be inserted by publisher] for [give brief description of material].
- [25] A. J. Magee, *Spin correlations in frustrated magnets with orbital ordering Ch.4* (Ph.D. thesis, Royal Holloway, University of London 2010).
- [26] G. J. MacDougall, V. O. Garlea, A. A. Aczel, H. D. Zhou, and S.E. Nagler, *Phys. Rev. B* **86**, 060414(R) (2012).
- [27] R. Nangneri and S. Y. Savrasov, *Phys. Rev. B* **86**, 085138 (2012).
- [28] T. Suzuki, M. Katsumura, K. Taniguchi, T. Arima, and T. Katsufuji, *Phys. Rev. Lett.* **98**, 127203 (2007).
- [29] J.-H. Chung, J.-H. Kim, S.-H. Lee, T. J. Sato, T. Suzuki, M. Katsumura, and T. Katsufuji, *Phys. Rev. B* **77**,

054412 (2008).

[30] S. T. Bramwell and M. J. Harris, *J. Phys. Condens. Matter* **10**, L215-L220 (1998).